



OPEN

SUBJECT AREAS:

SENSORS AND
BIOSENSORS

PHOTONIC DEVICES

Received
22 July 2014Accepted
8 December 2014Published
12 January 2015

Organic-on-silicon complementary metal–oxide–semiconductor colour image sensors

Seon-Jeong Lim^{1*}, Dong-Seok Leem^{1*}, Kyung-Bae Park^{1*}, Kyu-Sik Kim¹, Sangchul Sul², Kyoungwon Na², Gae Hwang Lee¹, Chul-Joon Heo¹, Kwang-Hee Lee¹, Xavier Bulliard¹, Ryu-Ichi Satoh¹, Tadao Yagi¹, Takkyun Ro¹, Dongmo Im², Jungkyu Jung², Myungwon Lee², Tae-Yon Lee², Moon Gyu Han¹, Yong Wan Jin¹ & Sangyoon Lee¹

¹Organic Materials Laboratory, Samsung Advanced Institute of Technology (SAIT), Samsung Electronics, Co. Ltd., 130 Samsung-ro, Yeongtong-gu, Suwon-si, Gyeonggi-do 443-803, Republic of Korea, ²System LSI, Samsung Electronics, Co. Ltd., 95 Samsung 2-ro, Giheung-gu, Yongin-si, Gyeonggi-do 446-711, Republic of Korea.

Correspondence and requests for materials should be addressed to M.G.H. (moongyu.han@samsung.com); Y.W.J. (ywj@ samsung.com) or S.L. (sangyoon.lee@samsung.com)

* These authors contributed equally to this work.

Complementary metal–oxide–semiconductor (CMOS) colour image sensors are representative examples of light-detection devices. To achieve extremely high resolutions, the pixel sizes of the CMOS image sensors must be reduced to less than a micron, which in turn significantly limits the number of photons that can be captured by each pixel using silicon (Si)-based technology (*i.e.*, this reduction in pixel size results in a loss of sensitivity). Here, we demonstrate a novel and efficient method of increasing the sensitivity and resolution of the CMOS image sensors by superposing an organic photodiode (OPD) onto a CMOS circuit with Si photodiodes, which consequently doubles the light-input surface area of each pixel. To realise this concept, we developed organic semiconductor materials with absorption properties selective to green light and successfully fabricated highly efficient green-light-sensitive OPDs without colour filters. We found that such a top light-receiving OPD, which is selective to specific green wavelengths, demonstrates great potential when combined with a newly designed Si-based CMOS circuit containing only blue and red colour filters. To demonstrate the effectiveness of this state-of-the-art hybrid colour image sensor, we acquired a real full-colour image using a camera that contained the organic-on-Si hybrid CMOS colour image sensor.

One method of doubling the surface area of a two-dimensional figure is to produce a three-dimensional, two-layer-stacked architecture within the same footprint. This principle can be applied to various novel conceptual and multidimensional optoelectronic devices, such as memory modules, displays, and complementary metal–oxide–semiconductor (CMOS) image sensors, to enhance their capacity, resolution, and sensitivity. Typical CMOS image sensors consist of two-dimensional colour filter arrays of blue (B), red (R), and green (G) pixels, *i.e.*, the Bayer filter pattern, in which the active area of the G colour filters is two times larger than that of the B and R colour filters¹. However, it is a great challenge to produce such typical CMOS image sensors with extremely high resolutions (pixel size < 1 μm) without any loss of sensitivity because of the smaller number of photons that can be captured by each pixel. To address this issue, the integration of CMOS image sensors with plasmonic colour filters^{2–5} or vertical silicon (Si) nanowires^{6,7} to serve as filter arrays has recently been reported. Nonetheless, such approaches have not yet provided the ultimate solution to the problem because the light-receiving area remains limited. Therefore, there is considerable demand for the realisation of the aforementioned concept of stacked architecture, in which a top photo-conversion layer serves as both a photodiode (PD) and a wavelength-selective colour filter, to achieve two-fold image acquisition capability. An organic photodiode (OPD) can be used for the top layer because organic semiconductor materials can be designed and tailored to absorb only a specific range of wavelengths of incident light. Although many attractive types of organic optoelectronic devices, including solar cells^{8–17}, PDs^{18–26}, and image sensors using colour filters^{27,28}, have been reported, there have been only a few examples of OPDs that exhibit wavelength-selective photo-conversion properties^{12,22,26}. In this paper, we present the first example of a multi-stacked organic-on-Si hybrid colour image sensor that consists of a G-light-selective OPD stacked on a newly designed Si-based CMOS circuit containing solely B and R colour filters.

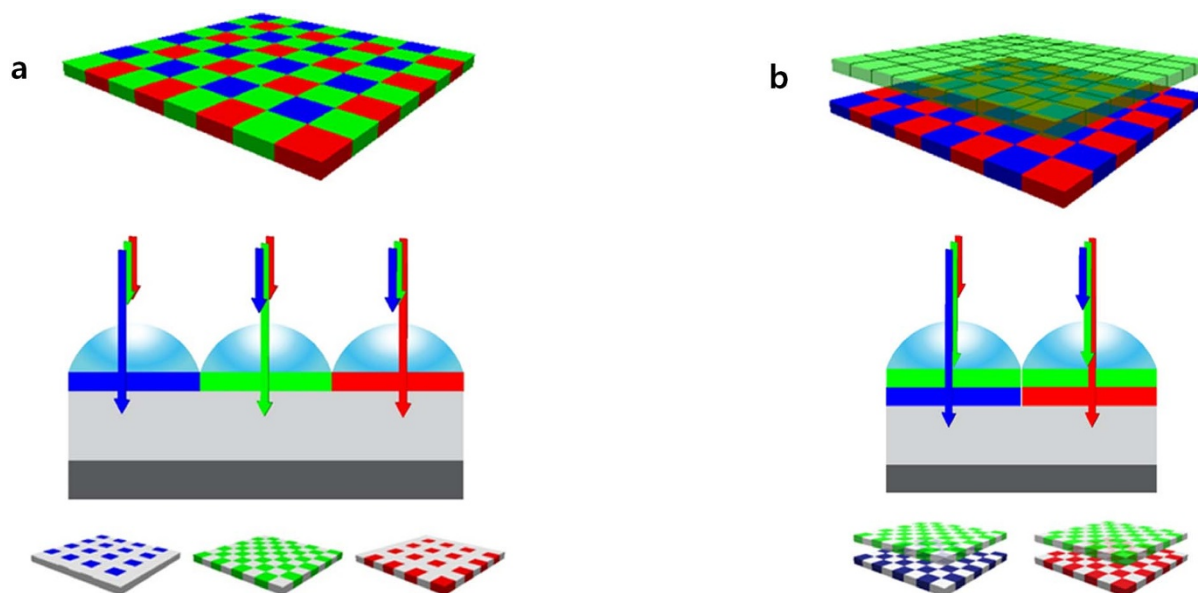


Figure 1 | Schematic diagrams of the CMOS colour image sensors. (a) A schematic diagram of a conventional two-dimensional CMOS colour image sensor. Each pixel measures the intensity of light passing through B, G, and R colour filters. In this side-by-side PD array, the area of the G colour filters is two times that of the B and R colour filters. (b) A schematic diagram of a three-dimensional, multi-stacked, organic-on-Si hybrid CMOS colour image sensor. A G OPD is placed on top of the B and R colour filters. The G OPD detects the amount of G light, after which the underlying Si PDs selectively detect the amounts of B and R light through the B and R colour filters, respectively.

A schematic diagram of the structure of the stacked organic-on-Si hybrid CMOS colour image sensor used in this work is presented in Fig. 1b for comparison with the conventional sensor depicted in Fig. 1a. As illustrated in this figure, a G-light-selective OPD, which converts only external G light into electrical signals, *i.e.*, electrons and holes, is used as the top photo-conversion layer to double the light-input surface area and to increase the sensitivity and resolution of the image sensor. In this configuration, the light-receiving area can be doubled with the same pixel size.

Results and Discussion

Green-light-absorbing organic semiconductor materials and thin films. Among quinacridone derivatives, which exhibit extreme resistance to irradiation with both heat and light and which exhibit excellent red colourant properties²⁹, 2,9-dimethylquinacridone (2,9-DMQA) possesses a two-dimensional intermolecular $\text{NH}\cdots\text{O}$ hydrogen bonding network in which the transition dipoles are aligned in a head-to-tail fashion³⁰. Consequently, these molecules exhibit excellent optoelectronic properties because of their effective intermolecular electronic coupling³¹. Therefore, various 2,9-DMQA derivatives with different alkyl chain lengths were synthesised (see Table 1 in the Supplementary Information for the list of candidates). Among these candidates, because of its high absorption capability, excellent thermal stability, and high-quality film morphology (Table 1, Supplementary Information), *N,N'*-dimethyl-2,9-dimethylquinacridone (DM-2,9-DMQA) was used as an electron-donor (p-type) material in this work, as shown in Fig. 2a. DM-2,9-DMQA was synthesised *via* the methylation of 2,9-DMQA, and its molecular structure was completely characterized *via* nuclear magnetic resonance (NMR) spectroscopy, mass spectroscopy, and elemental analysis (see the Methods section). DM-2,9-DMQA possesses a highly symmetric and cyclic molecular structure and exhibits a narrow absorption spectrum in the G wavelength region (absorption coefficient (α) = $0.40 \times 10^5 \text{ cm}^{-1}$ at $\lambda^{\text{abs.film}}_{\text{max}} = 546 \text{ nm}$, full width at half maximum (FWHM) = 60 nm) when in the form of a thermally evaporated thin film under high vacuum ($<10^{-7}$ Torr) (see the Methods section for details of the thin-film fabrication), as shown in Fig. 2c. The effective intermolecular π - π

electronic coupling of DM-2,9-DMQA in a thin film results in an apparent bathochromic shift in the ground-state absorption ($\lambda^{\text{abs.soln}}_{\text{max}} = 531 \text{ nm}$ versus $\lambda^{\text{abs.film}}_{\text{max}} = 546 \text{ nm}$) and a significant fluorescence quenching (photoluminescence (PL) quantum yield (Φ)_{solution} = 80% at $2.7 \times 10^{-5} \text{ M}$ versus $\Phi_{\text{film}} = 0.7\%$) with a strong bathochromic shift ($\lambda^{\text{em.soln}}_{\text{max}} = 555 \text{ nm}$ versus $\lambda^{\text{em.film}}_{\text{max}} = 616 \text{ nm}$), as shown in Figs. 2b and c. Hence, the stacking order of DM-2,9-DMQA in a thin film is quite similar to that observed in single-crystalline *N,N'*-dimethylquinacridone (DMQA), which exhibits a quasi-head-to-tail arrangement of transition dipoles³². Compared with DMQA, however, DM-2,9-DMQA exhibits superior optoelectronic properties when in the form of a thermally evaporated thin film, meaning that DM-2,9-DMQA is a more useful electron-donor (p-type) semiconductor material (Table 1, Supplementary Information). Boron subphthalocyanine chloride (SubPc) was selected for use as the electron-acceptor (n-type) material in the OPD for this study (Fig. 2d) because of its high absorption coefficient and specific absorption characteristics in the G wavelength region ($\alpha = 1.42 \times 10^5 \text{ cm}^{-1}$ at $\lambda^{\text{abs.film}}_{\text{max}} = 586 \text{ nm}$, FWHM = 79 nm; $\Phi_{\text{film}} = 2.1\%$, $\lambda^{\text{em.film}}_{\text{max}} = 617$ and 717 nm) when in the form of a thermally evaporated thin film (Fig. 1, Supplementary Information)³³. The energy levels of the highest occupied molecular orbitals (HOMOs) and those of the lowest unoccupied molecular orbitals (LUMOs) of both molecules in thin-film form are presented in Fig. 2e (see the Methods section for details regarding the measurement of these energy levels). Based on the energy levels of the HOMOs and LUMOs of the molecules, we hypothesised that it should be possible to form an effective bulk heterojunction (BHJ) in a blended film prepared *via* thermal co-evaporation under high vacuum (Fig. 2f; $\alpha = 0.97 \times 10^5 \text{ cm}^{-1}$ at $\lambda^{\text{abs.film}}_{\text{max}} = 580 \text{ nm}$, FWHM = 85 nm; $\Phi_{\text{film}} = 0.5\%$, $\lambda^{\text{em.film}}_{\text{max}} = 619 \text{ nm}$).

Transient absorption spectroscopy and mobility in the blend. To examine the formation of excitons and the charge separation in the BHJ under irradiation with external G light, transient absorption spectroscopy (TAS) measurements of the BHJ film were performed, as shown in Fig. 2g. The dynamics of the ground-state

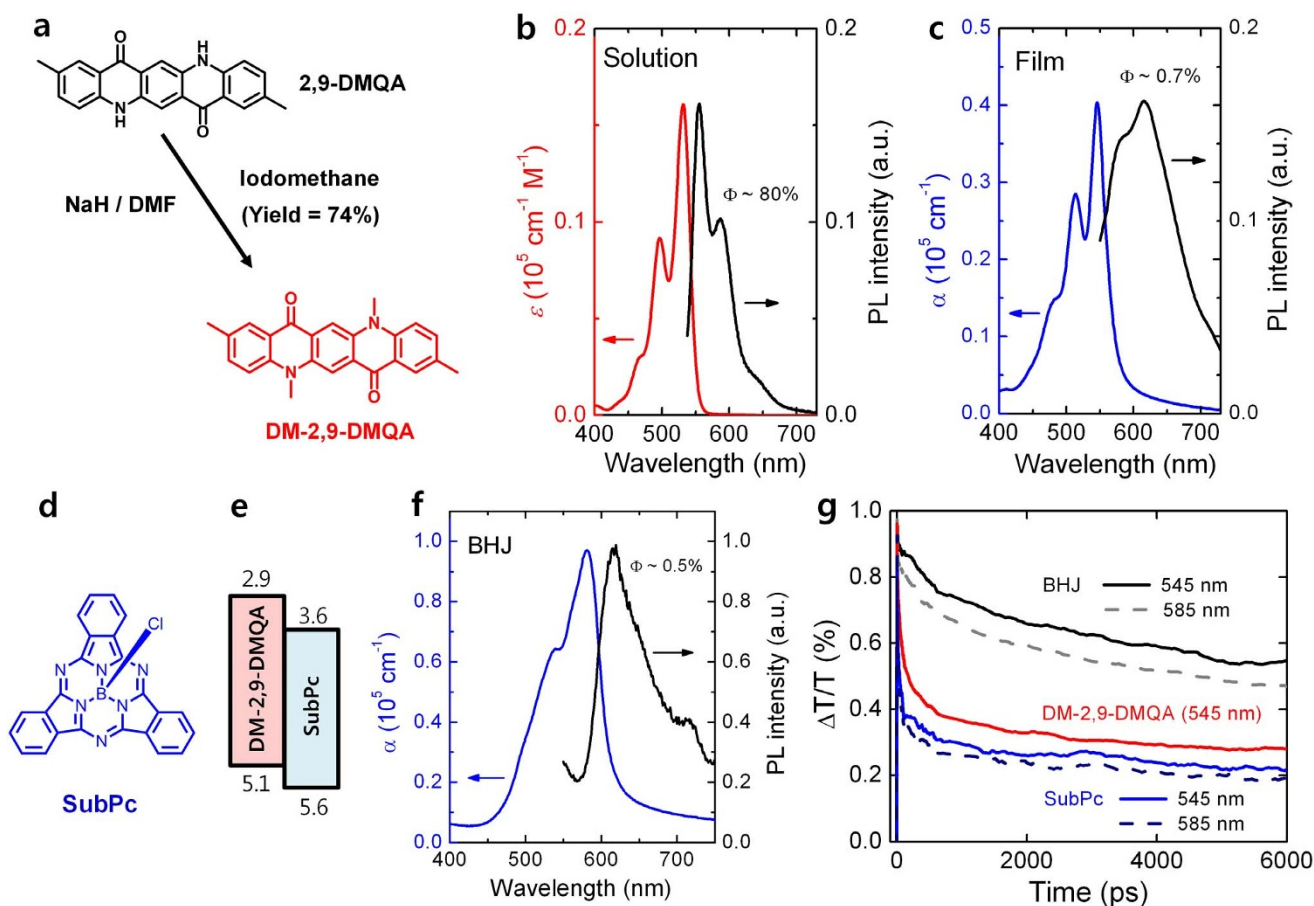


Figure 2 | Preparation of organic semiconductor materials and the characteristics of the thin films. (a) Synthesis and molecular structure of DM-2,9-DMQA. (b) UV-visible absorption (red line) and PL (black line) spectra of DM-2,9-DMQA dissolved in chloroform solution; the molar absorption coefficient (ϵ) = $0.16 \times 10^5 \text{ cm}^{-1} \text{ M}^{-1}$ at $\lambda_{\text{max}} = 531 \text{ nm}$. (c) UV-visible absorption (blue line) and PL (black line) spectra of a DM-2,9-DMQA thin film fabricated *via* thermal evaporation under high vacuum; the absorption coefficient (α) = $0.40 \times 10^5 \text{ cm}^{-1}$ at $\lambda_{\text{max}} = 546 \text{ nm}$. (d) Molecular structure of SubPc. (e) HOMO and LUMO energy levels of thin films of DM-2,9-DMQA and SubPc. (f) UV-visible absorption (blue line) and PL (black line) spectra of a BHJ (DM-2,9-DMQA : SubPc = 1 : 1) film. (g) TAS spectra of DM-2,9-DMQA (red line), SubPc (blue lines), and blend BHJ (DM-2,9-DMQA : SubPc = 1 : 1) (black lines) films. The bi-exponential time constants (τ) are as follows: for DM-2,9-DMQA, $\tau_1 = 34 \text{ ps}$ and $\tau_2 = 640 \text{ ps}$ at 545 nm; for SubPc, $\tau_1 = 25 \text{ ps}$ and $\tau_2 = 870 \text{ ps}$ at 545 nm, $\tau_1 = 10 \text{ ps}$ and $\tau_2 = 460 \text{ ps}$ at 585 nm; and for blend BHJ, $\tau_1 = 210 \text{ ps}$ and $\tau_2 = 2800 \text{ ps}$ at 545 nm, $\tau_1 = 12 \text{ ps}$ and $\tau_2 = 4400 \text{ ps}$ at 585 nm.

bleaching (GSB) band at 545 and 585 nm for pristine DM-2,9-DMQA and SubPc and for the BHJ blend (DM-2,9-DMQA : SubPc = 1 : 1, 70 nm) revealed ultrafast photo-induced charge transfer in the BHJ, which could be described by bi-exponential terms^{10,17}. The GSB profile of the BHJ exhibited a decay profile that was considerably more delayed than those of the pristine DM-2,9-DMQA and SubPc single layers, implying slower charge recombination, and the response remained nearly constant in the nanosecond time regime. This slow charge recombination in the BHJ was expected to give rise to highly efficient OPD performance. Further analysis of the charge-carrier mobility in the BHJ was performed using the space-charge-limited current (SCLC) method¹¹, from which the zero-field mobilities for holes and electrons were found to be $4.5 \times 10^{-10} \text{ cm}^2/\text{Vs}$ and $5.6 \times 10^{-9} \text{ cm}^2/\text{Vs}$, respectively (see the Methods section and Fig. 2 in the Supplementary Information). However, when an electric field was applied to the device, the charge-carrier mobilities increased to $2.1 \times 10^{-7} \text{ cm}^2/\text{Vs}$ and $2.0 \times 10^{-7} \text{ cm}^2/\text{Vs}$ at 0.3 MV/cm for holes and electrons, respectively, which are 2–3 orders of magnitude higher than the corresponding zero-field mobilities.

Characteristics of green-light-selective OPDs. To characterise the optoelectronic properties of the BHJ and to investigate the possibility

of using the BHJ as the top G-light-selective OPD in the proposed image sensor structure (Fig. 1b), a device consisting of an indium tin oxide (ITO)-coated glass substrate, a hole-extraction layer of molybdenum oxides (MoO_x), a BHJ of DM-2,9-DMQA and SubPc, and an aluminium (Al) contact was fabricated (see the Methods section and Fig. 3a in the Supplementary Information). The device performance in terms of efficiency was then optimised by varying the mixing ratios of DM-2,9-DMQA in the blends and the thicknesses of the BHJ. The optimal structure was found to be a 70-nm-thick BHJ with a mixing ratio of 45–60% DM-2,9-DMQA in the blend (see Fig. 3b in the Supplementary Information for the efficiency contour plots). Representative current density–voltage (J - V) curves characteristic of an OPD with a 70-nm-thick BHJ and a blend ratio of 1 : 1 under both dark and illuminated conditions are presented in Fig. 3a. The diode exhibited a relatively low dark-current density (J_d) of 53 nA/cm² at a reverse bias of -3 V , which was the operating voltage used in this study. Furthermore, the diode exhibited a high injection current of $4.5 \times 10^{-3} \text{ A/cm}^2$ at a forward bias of 3 V, leading to a high rectification ratio of 8.49×10^4 at $\pm 3 \text{ V}$. The device also responded to external G light ($\lambda_{\text{max}} = 553 \text{ nm}$), and the response behaviour of the photocurrent density (J_{ph}) versus the light intensity (I) exhibited good linearity. The spectral responsivity (R) of the OPD was also evaluated as presented in Fig. 3b (see the



Methods section). The OPD without any external reverse bias exhibited a relatively low R_{max} of 0.092 A/W at a wavelength of 580 nm, whereas it exhibited a highly enhanced R_{max} of 0.264 A/W when a reverse bias of -3 V was applied. A figure of merit known as the specific detectivity (D^*) was evaluated using the expression $D^* = R/(2qJ_d)^{0.5}$, from which a high D^* of 2.03×10^{12} cm Hz^{1/2} W⁻¹ was obtained at a wavelength of 580 nm under a reverse bias of -3 V. In this estimation, the shot noise from the dark current was considered to be the major contributor to the total noise of the OPD²³. Furthermore, the OPD driven by the -3 V bias exhibited a remarkably high selectivity to external G light, displaying a FWHM as narrow as 115 nm, which can be attributed to the narrow absorption profile of the BHJ formed of DM-2,9-DMQA and SubPc, resulting in a strong *sympatric* response¹⁹. Plots of the external quantum efficiency (EQE) as a function of the applied reverse biases are presented in Fig. 3c. At low reverse biases (<-1 V), relatively low EQEs of less than 40% were obtained, which resulted primarily from the slow charge-carrier mobilities¹⁶. However, a further increase in the reverse bias led to a drastic improvement in the efficiency, with EQEs of 56.5% and 75.8% at reverse biases of -3 V and -10 V, respectively. These enhanced values are attributed to the electric-field-aided enhancement of the charge-carrier mobilities and transport (collection) efficiencies, leading to the consequent minimisation of charge recombination loss, as previously described¹³. Furthermore, the internal quantum efficiency (IQE) was estimated to be as high as 69.8% (-3 V) or 93.7% (-10 V) based on the calculated absorbance of the BHJ

(i.e., 81.3% at 580 nm). The speed of the photo-response, which is critical in OPDs that are used for imaging purposes³⁴, is demonstrated in Fig. 3d. The -3 dB frequency, at which the amplitude of the photocurrent decreased to $1/\sqrt{2}$ of its initial value³⁴, was measured to be 76.7 kHz for the OPD driven at a -3 V bias. Rapid rise (4.34 μ s) and fall (4.42 μ s) times were also obtained for the device at the -3 dB frequency (Fig. 3d inset). Further analysis of the thermal stability of the OPD, which was performed by annealing the device at increasing temperatures of up to 140°C for 30 min at each temperature, revealed only a 3.6% drop in the EQE measured at -3 V (Fig. 3e). This high thermal stability was strongly supported by the ultraviolet (UV)-visible absorption spectra and atomic force microscopy (AFM) images of the BHJ (DM-2,9-DMQA:SubPc = 1:1) blend film (see Fig. 4, Supplementary Information), which revealed no significant change after thermal annealing. These results strongly suggest that a BHJ consisting of DM-2,9-DMQA and SubPc organic semiconductors can be used as the key element of the top G-light-selective OPD in the proposed image sensor structure (Fig. 1b).

Transparent inverted-structure OPDs. To realise the organic-on-Si hybrid CMOS colour image sensor, a G OPD with transparent ITO electrodes on both sides was fabricated using the same BHJ (DM-2,9-DMQA:SubPc = 1:1, 90 nm) (Fig. 4a inset)^{35,36}. This inverted-structure G OPD exhibited a fairly high transmittance ($\sim 70\%$) for wavelengths in the B and R regions (Fig. 4a), which provided an excellent pathway for the incident B and R light to pass through

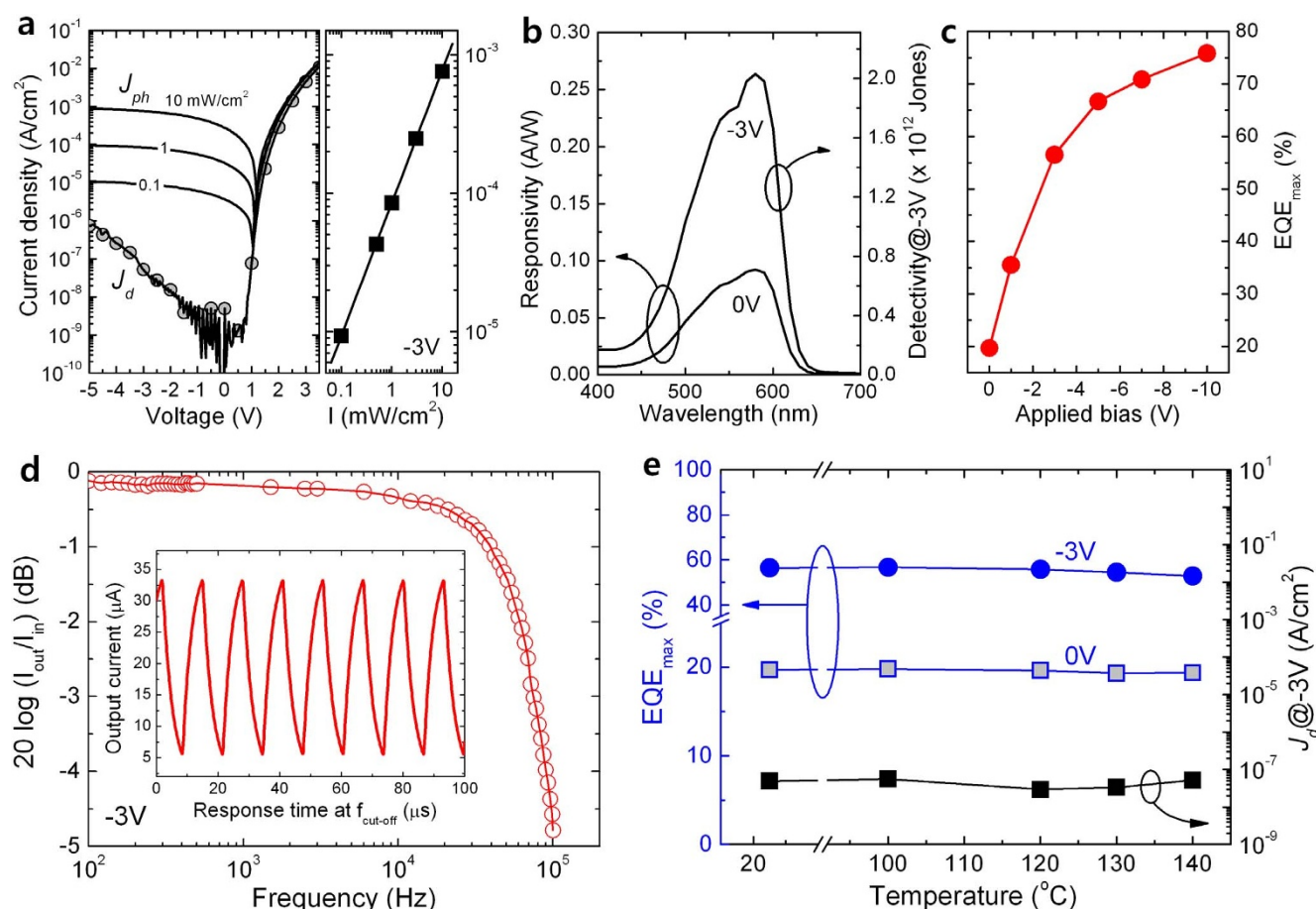


Figure 3 | Properties of a normal-structure OPD with a BHJ (DM-2,9-DMQA : SubPc ratio = 1 : 1, thickness = 70 nm). (a) Current density–voltage (J – V) curves under dark and illuminated ($\lambda_{max} = 553$ nm) conditions (0.1–10 mW/cm²). The right-hand figure reveals good linearity in the behaviour of the photocurrent density (J_{ph}) versus the light intensity (I). (b) Responsivity and detectivity as functions of the wavelength of incident light obtained at bias values of 0 and -3 V. (c) Change in EQE versus applied bias. (d) Response time as a function of frequency. (e) Thermal stability evaluated by the changes in the EQE and dark current with increasing temperature.



the G OPD, thereby permitting the B and R light to be detected by the bottom Si PDs driven by CMOS circuits. When considering the reflection from the top encapsulation glass layer and from the device, only approximately 10% of the external B and R light were absorbed by this transparent G OPD (Fig. 4a). Despite the lower maximum EQE (41.2%) exhibited by this transparent G OPD at a wavelength of 580 nm compared with the value exhibited by the G OPD that was fabricated using an Al electrode, the EQEs of the BGR PDs were perfectly balanced (Fig. 4b). Furthermore, the total number of charges generated in each pixel was calculated to be 1.6 times higher than that in conventional systems (see Fig. 5, Supplementary Information), which is attributed to the increased light-receiving area of our novel image sensor structure.

Organic-on-Si CMOS colour image sensors. The transparent inverted-structure G OPDs were fully integrated onto CMOS chips (see the Methods section for details). Fig. 4c presents a cross-sectional transmission electron microscopy (TEM) image of the organic layers sandwiched between the bottom and top ITO electrodes, *i.e.*, the transparent G OPD structure. Furthermore, the inset of Fig. 4c presents a tiled scanning electron microscopy (SEM) image of the bottom ITO arrays. The aforementioned transparent inverted-structure G OPD used to acquire the G signal was stacked

on top of a novel front-side-illumination-type CMOS circuit designed to respond to solely B and R light. A representative output signal curve from the top G OPD pixels is plotted in Fig. 4d, which clearly reveals a linear response to illumination at a reverse bias of 3 V. The sensitivity of these G pixels, as calculated from the slope of the output signal versus the illumination intensity, was 250 mV/lux·sec. This result indicates highly well connected operation between the top G OPD pixels and the bottom CMOS circuit, which facilitated the flow of electrons from the G OPD pixels to the CMOS circuit for colour modulation. The thermal budget of a CMOS image sensor under biased conditions at elevated temperatures is important for switching in CMOS-driven sensors. As shown in Fig. 4e, the output signal under illumination at 120 lux (3.2×10^4 mV/sec) remained constant regardless of thermal stresses from room temperature (25°C) to 140°C under a reverse bias of 3 V. In addition, the output signal without illumination (*i.e.*, in darkness) was as low as 45 mV/sec after thermal treatment at temperatures of up to 140°C, maintaining a signal contrast of three orders of magnitude between the signal produced under illumination at 120 lux and that produced under dark conditions at a reverse bias of 3 V (Fig. 4e). The high linearity in the output signal and the excellent thermal stability of the G OPD pixels confirmed the successful fabrication of a novel multi-stacked organic-on-Si

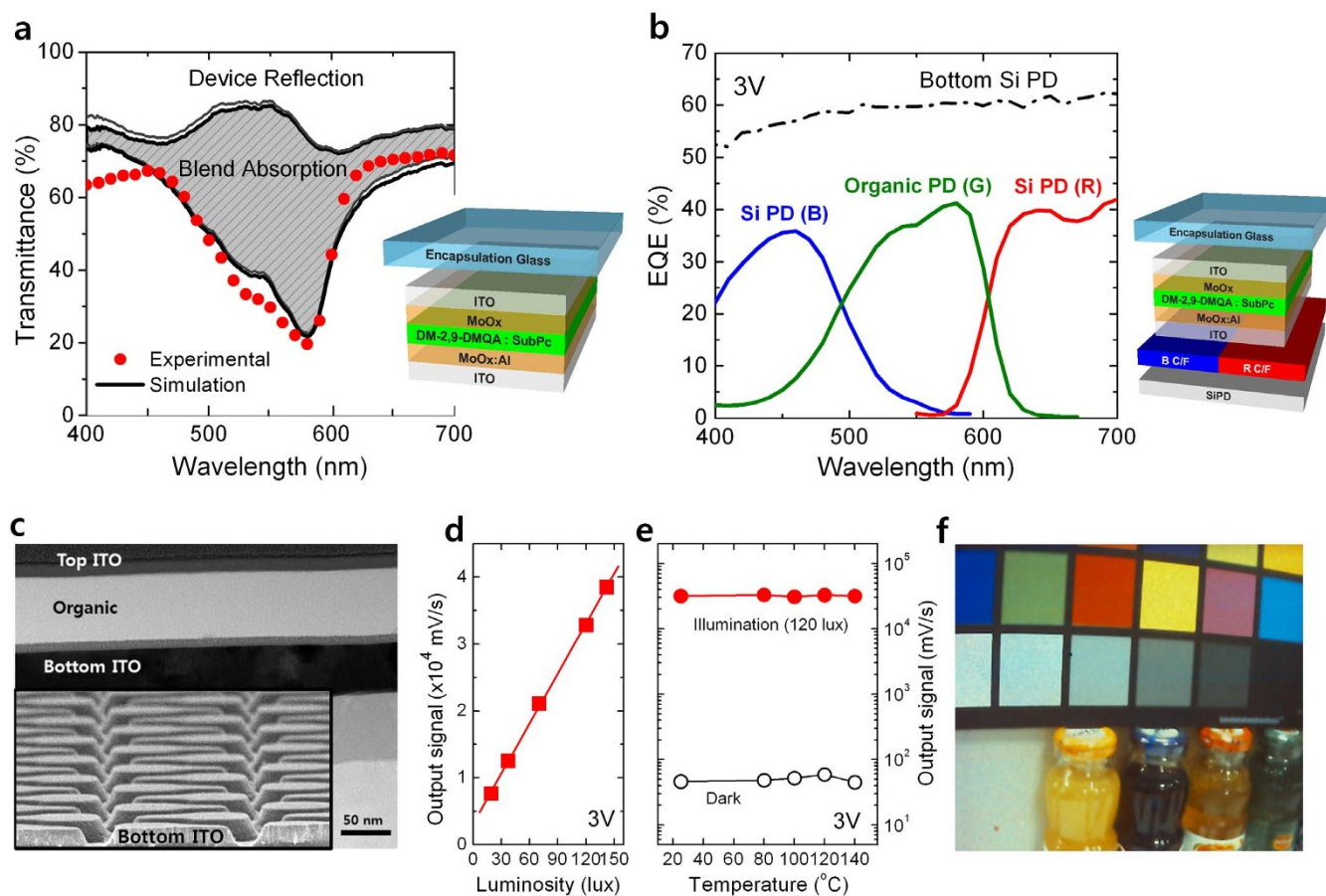


Figure 4 | Properties of a transparent inverted-structure OPD with a BHJ (DM-2,9-DMQA : SubPc ratio = 1 : 1, thickness = 90 nm) (a, b). (a) Transmittance of the device both experimentally measured and calculated by optical simulation using the n and k values of the BHJ. The red dots represent experimental values and the shaded area represents light absorption by the BHJ. (b) EQE curves of B, G, and R PDs. The EQEs of the B and R regions were measured in the underlying Si PDs, on which the B or R colour filters and the transparent G OPD were physically stacked. The EQE of the transparent G OPD was measured directly at an operating voltage of 3 V. Actual organic-on-Si hybrid CMOS colour image sensors (c–f). (c) Cross-sectional TEM and SEM (inset) images of the hybrid CMOS colour image sensor array of G OPD pixels. The B and R colour filters and the CMOS circuit with Si PDs are located under the bottom ITO array. (d) Output signal as a function of light intensity in G OPD pixels at a bias of 3 V. (e) Thermal stability of the output signal under illumination at 120 lux and in the dark state in G OPD pixels at a bias of 3 V. (f) A full-colour image acquired using a camera integrated with a 5-megapixel organic-on-Si hybrid CMOS colour image sensor.



hybrid CMOS colour image sensor. Hence, this technology can potentially pave the way towards the doubled sensitivity of colour image sensors for a given pixel size. Fig. 4f presents a full-colour, 5-megapixel image acquired using a camera containing the hybrid CMOS colour image sensor fabricated in this study (Table 2, Supplementary Information). The elementary colours B, G, and R are distinct, and the white is perfectly balanced because of the balance among the EQEs of the BGR sensors, as shown in Fig. 4b. Additionally, the quality of the images acquired using the camera containing this hybrid colour image sensor remained stable, without any loss of sensitivity throughout the SAMSUNG Tech. Fair 2013, over one week of continuous irradiation with room light.

Conclusion

A BHJ consisting of DM-2,9-DMQA and SubPc organic semiconductors was fabricated and found to satisfy the requirements for use in a double-stacked hybrid colour image sensor, with highly G-light-selective absorption properties, high photo-conversion efficiency, excellent thermal stability, and rapid response characteristics. This BHJ was used as the key element in G-light-selective OPDs. By integrating a transparent inverted-structure G OPD onto a newly designed CMOS circuit containing only B and R colour filters, we developed a novel stacked organic-on-Si hybrid CMOS colour image sensor. We also demonstrated the reliability of this architecture: a real full-colour image (5 megapixels) was successfully acquired using a camera that contained this hybrid colour image sensor. Higher-quality organic-on-Si hybrid CMOS colour image sensors can be successfully manufactured by increasing the sensitivity of the top G OPD and through further architectural modification of the bottom CMOS circuit. These next-generation multi-stacked organic-on-Si hybrid colour image sensors are highly promising in terms of sensitivity and resolution because they can guarantee the doubling of the light-input surface area within a given pixel footprint.

Methods

Instrumentation. ^1H -NMR and ^{13}C -NMR spectra were obtained using a Bruker Avance III 600 (600 MHz) instrument with CDCl_3 as the solvent. Matrix-assisted laser desorption/ionization–time of flight (MALDI-TOF) mass spectra were recorded using an Ultraflex III TOF/TOF 200 system, and mass spectra were measured using a TOF LC/MS (Shimadzu) in ESI positive mode. Elemental analysis was performed using a PE 2400 Series II analyser. UV-visible absorption spectra were acquired using a Varian Cary 500 Bio spectrophotometer. Absolute PL quantum yields were measured using a Quantaurus-QY spectrometer (Hamamatsu C11347). Cross-sectional transmission electron microscopy (TEM) (Tecnai G2ST) and scanning electron microscopy (SEM) (Hitachi SU-8030) images were acquired using the focused ion beam (FIB) (Helios NanoLab 400S) milling technique. The HOMO levels of all organic thin films were measured using an AC-2 photoelectron spectrophotometer (Hitachi High Tech). The LUMO levels were determined from the optical band gap calculated from the edge of the absorption spectra. The current density–voltage (J - V) characteristics of the OPDs were measured using a Keithley K4200 parameter analyser. The photocurrent characteristics were evaluated under illumination with a G laser diode ($\lambda_{\text{max}} = 553$ nm) at various light intensities in the range of 0.1–10 mW/cm 2 . EQEs were measured using an instrumental setup illuminated with monochromatic light generated by an ozone-free xenon lamp with a chopper frequency of 30 Hz. The monochromatic light intensity was calibrated using a Si photodiode (Hamamatsu S1337). The corresponding R (A/W), defined as the ratio of the generated photocurrent (A) to the incident light power (W), was calculated from the EQE using the relation $R = \text{EQE}/h\nu$, where $h\nu$ is the incident photon energy in electron volts (eV). The frequency response was evaluated using a measurement setup consisting of an oscilloscope with a bandwidth of 500 MHz (LeCroy Wavejet 352A), an AFG-2125 function generator (GW Instek), and a G laser diode ($\lambda_{\text{max}} = 553$ nm, power = 10 mW/cm 2).

Synthesis of N,N' -dimethyl-2,9-dimethylquinacridone (DM-2,9-DMQA). To a mixture of 2,9-dimethylquinacridone (1 mmol) in distilled dimethyl formamide (DMF) (20 mL) was added NaH (60% oil dispersion, 5 mmol) at 0°C. The reaction mixture was stirred at 60°C for 30 min and cooled to room temperature under continuous stirring, after which iodomethane (5 mmol) was added. The mixture was further stirred at 60°C for 18 h and was then quenched with H_2O . The resulting solid was collected *via* filtration and was thoroughly washed with H_2O to afford a reddish orange solid. The solid product was further purified *via* column chromatography on silica gel (chloroform/methanol = 9/1). The resulting product was recrystallised twice from dichloromethane/hexanes (yield = 74%). Melting point > 325°C. ^1H -

NMR (CDCl_3 , 600 MHz): δ 8.79 (s, 2H), δ 8.38 (s, 2H), δ 7.61 (d, 2H, $J = 8.8$ Hz), δ 7.50 (d, 2H, $J = 8.9$ Hz), δ 4.07 (s, 6H), δ 2.51 (s, 6H). ^{13}C -NMR (CDCl_3 , 600 MHz): δ 178.41, 141.56, 136.73, 136.26, 130.75, 127.41, 126.34, 121.32, 114.87, 113.58, 34.07, 20.74. MALDI-TOF mass: 368 (m/z). HRMS (ESI $^+$): calculated for $\text{C}_{24}\text{H}_{21}\text{N}_2\text{O}_2$ [$M + \text{H}^+$]: 369.1603; found: 369.1601. Elemental analysis: calculated for $\text{C}_{24}\text{H}_{20}\text{N}_2\text{O}_2$: C - 78.24%, H - 5.47%, N - 7.60%, O - 8.69%; found: C - 78.16%, H - 5.46%, N - 7.59%, O - 8.79%.

Boron subphthalocyanine chloride (SubPc). This material was purchased from commercial suppliers (sublimed grade, Luminescence Technology Corp.) and used as received.

Fabrication of organic thin films. All organic semiconductor materials were purified *via* sublimation under high vacuum ($<10^{-6}$ Torr) prior to use. Thin films were fabricated *via* thermal evaporation under high vacuum ($<10^{-7}$ Torr) at a rate of 0.5–1.0 Å/s on dried glass or quartz substrates that had been cleaned with isopropyl alcohol (IPA) and acetone in an ultrasonic cleaner.

Fabrication of OPDs. The normal-structure OPDs were fabricated on ITO-coated glass substrates by sequentially depositing a 30-nm-thick hole-extraction layer of MoO_x , a 70- to 90-nm-thick organic BHJ layer of DM-2,9-DMQA : SubPc, and an 80-nm-thick Al electrode. The mixing ratios were varied by modifying the concentration of DM-2,9-DMQA in the BHJ blend. All film layers were thermally evaporated under high vacuum ($<10^{-7}$ Torr) and the devices were finally encapsulated with glass (transmittance = 90%). The active pixel size, defined by the orthogonal overlap of the two electrodes, was 0.04 cm 2 . To extract the hole and electron charge-carrier mobilities of the BHJ using the SCLC method, single-carrier devices consisting of ITO/ MoO_x (30 nm)/DM-2,9-DMQA : SubPc (1 : 1 ratio, 70 nm thickness)/ MoO_x (20 nm)/Al (80 nm) (hole-only device) and ITO/ MoO_x : Al (5 nm)/DM-2,9-DMQA : SubPc (1 : 1 ratio, 70 nm thickness)/Al (80 nm) (electron-only device) were fabricated. Transparent inverted-structure OPDs were fabricated on cleaned ITO-coated glass substrates by sequentially depositing a 5-nm-thick electron-extraction layer of MoO_x : Al, a 90-nm-thick organic BHJ layer of DM-2,9-DMQA : SubPc (1 : 1), a 10-nm-thick hole-extraction layer of MoO_x , and an ITO electrode using a sputter system. Then, the OPDs were encapsulated with glass (transmittance = 90%). The active pixel size, defined by the orthogonal overlap of the two ITO electrodes, was 0.04 cm 2 .

Fabrication of the double-stacked organic-on-Si hybrid colour image sensor. A newly designed front-side-illumination-type CMOS image sensor circuit (5 megapixels) containing only B and R colour filters was used to acquire B and R signals. An oxide-barrier pixel array was formed on the top metal layer for the process of B and R colour filters. The extruded portions of the B and R colour filters were removed using the chemical-mechanical-polishing (CMP) technique. The bottom ITO electrodes were patterned and connected to the underlying metal layer of the CMOS circuit through holes surrounded by the low-temperature CVD oxide, which was also planarised *via* additional CMP. The dimensions of the patterned ITO were equivalent to a pixel pitch of 1.4 μm . Then, a transparent inverted-structure OPD was fabricated by sequentially depositing MoO_x : Al (5 nm)/DM-2,9-DMQA : SubPc (1 : 1 ratio, 90 nm thickness)/ MoO_x (10 nm)/ITO *via* thermal evaporation and sputtering. Finally, the organic-on-Si hybrid colour image sensor was encapsulated with glass.

- Ohta, J. *Smart CMOS image sensors and applications*. (CRC Press: Florida, USA, 2007).
- Yokogawa, S., Burgos, S. P. & Atwater, H. A. Plasmonic color filters for CMOS image sensor applications. *Nano Lett.* **12**, 4349–4354 (2012).
- Burgos, S. P., Yokogawa, S. & Atwater, H. A. Color imaging *via* nearest neighbor hole coupling in plasmonic color filters integrated onto a complementary metal-oxide semiconductor image sensor. *ACS Nano* **7**, 10038–10047 (2013).
- Zeng, B., Gao, Y. & Bartoli, F. J. Ultrathin nanostructured metals for highly transmissive plasmonic subtractive color filters. *Sci. Rep.* **3**, 2840 (2013).
- Berini, P. Surface plasmon photodetectors and their applications. *Laser Photon. Rev.* **8**, 197–220 (2014).
- Park, H. & Crozier, K. B. Multispectral imaging with vertical silicon nanowires. *Sci. Rep.* **3**, 2460 (2013).
- Park, H. *et al.* Filter-free image sensor pixels comprising silicon nanowires with selective color absorption. *Nano Lett.* **14**, 1804–1809 (2014).
- Tang, C. W. Two-layer organic photovoltaic cell. *Appl. Phys. Lett.* **48**, 183–185 (1986).
- Yu, G., Gao, J., Hummelen, J. C., Wudl, F. & Heeger, A. J. Polymer photovoltaic cells: Enhanced efficiencies *via* a network of internal donor-acceptor heterojunctions. *Science* **270**, 1789–1791 (1995).
- Hwang, I.-W. *et al.* Ultrafast electron transfer and decay dynamics in a small band gap bulk heterojunction material. *Adv. Mater.* **19**, 2307–2312 (2007).
- Lenes, M., Morana, M., Brabec, C. J. & Blom, P. W. M. Recombination-limited photocurrents in low bandgap polymer/fullerene solar cells. *Adv. Funct. Mater.* **19**, 1106–1111 (2009).
- Meiss, J. *et al.* Tetrabutyl-tetraphenyl-diindenoperylene derivatives as alternative green donor in bulk heterojunction organic solar cells. *Sol. Energy. Mat. Sol. Cells* **95**, 630–635 (2011).



13. Tress, W., Leo, K. & Riede, M. Optimum mobility, contact properties, and open-circuit voltage of organic solar cells: A drift-diffusion simulation study. *Phys. Rev. B* **85**, 155201-1–155201-11 (2012).
14. Congreve, D. N. *et al.* External quantum efficiency above 100% in a singlet-exciton-fission-based organic photovoltaic cell. *Science* **340**, 334–337 (2013).
15. Janssen, R. A. J. & Nelson, J. Factors limiting device efficiency in organic photovoltaics. *Adv. Mater.* **25**, 1847–1858 (2013).
16. Faist, M. A. *et al.* Understanding the reduced efficiencies of organic solar cells employing fullerene multiadducts as acceptors. *Adv. Energy Mater.* **3**, 744–752 (2013).
17. Rao, A. *et al.* The role of spin in the kinetic control of recombination in organic photovoltaics. *Nature* **500**, 435–440 (2013).
18. Halls, J. J. M. *et al.* Efficient photodiode from interpenetrating polymer networks. *Nature* **376**, 498–500 (1995).
19. Harrison, M. G., Grüner, J. & Spencer, G. C. W. Analysis of the photocurrent action spectra of MEH-PPV polymer photodiodes. *Phys. Rev. B* **55**, 7831–7849 (1997).
20. Someya, T. *et al.* Integration of organic FETs with organic photodiodes for a large area, flexible, and lightweight sheet image scanners. *IEEE Trans. Electron Devices* **52**, 2502–2511 (2005).
21. Wang, X. *et al.* Integrated thin-film polymer/fullerene photodetectors for on-chip microfluidic chemiluminescence detection. *Lab Chip* **7**, 58–63 (2007).
22. Seo, H. *et al.* Color sensors with three vertically stacked organic photodetectors. *Jpn. J. Appl. Phys.* **46**, L1240–L1242 (2007).
23. Gong, X. *et al.* High-detectivity polymer photodetectors with spectral response from 300 nm to 1450 nm. *Science* **325**, 1665–1667 (2009).
24. Rauch, T. *et al.* Near-infrared imaging with quantum-dot-sensitized organic photodiodes. *Nat. Photon.* **3**, 332–336 (2009).
25. Baierl, D. *et al.* A hybrid CMOS-imager with a solution-processable polymer as photoactive layer. *Nat. Commun.* **3**, 1175 (2012).
26. Vuuren, R. D. J., Pivrikas, A., Pandey, A. K. & Burn, P. L. Colour selective organic photodetectors utilizing ketocyanine-cored dendrimers. *J. Mater. Chem. C* **1**, 3532–3543 (2013).
27. Yu, G., Cao, Y., Wang, J., McElvain, J. & Heeger, A. J. High sensitivity polymer photosensors for imaging sensing applications. *Synth. Met.* **102**, 904–907 (1999).
28. Ihama, M. *et al.* CMOS image sensor with an overlaid organic photoelectric conversion layer: Optical advantages of capturing slanting rays of light. P33 presented at 2011 International Image Sensor Workshop (IISW): Session 04, Hokkaido, Japan. California, USA: International Image Sensor Society (IIS). (2011, June 8).
29. Herbst, W. & Hunger, K. *Industrial organic pigments: Production, properties, applications.* (3rd ed., VCH: Weinheim, Germany, 2004).
30. Senju, T., Nishimura, N. & Mizuguchi, J. Polymorph of 2,9-dichloroquinacridone and its electronic properties. *J. Phys. Chem. A* **111**, 2966–2970 (2007).
31. Fitzner, R. *et al.* Interrelation between crystal packing and small-molecule organic solar cell performance. *Adv. Mater.* **24**, 675–680 (2012).
32. Mizuguchi, J. & Senju, T. Solution and solid-state spectra of quinacridone derivatives as viewed from the intermolecular hydrogen bond. *J. Phys. Chem. B* **110**, 19154–19161 (2006).
33. Beaumont, N. *et al.* Boron subphthalocyanine chloride as an electron acceptor for high-voltage fullerene-free organic photovoltaics. *Adv. Funct. Mater.* **22**, 561–566 (2012).
34. Shinar, R. & Shinar, J. *Organic electronics in sensors and biotechnology.* Ch. 6. (McGraw-Hill Professional: New York, USA, 2009).
35. Schmidt, H. *et al.* Efficient semitransparent inverted organic solar cells with indium tin oxide top electrode. *Appl. Phys. Lett.* **94**, 243302-1–243302-3 (2009).
36. Liu, J. *et al.* High-efficiency inverted polymer solar cells with transparent and work-function tunable MoO₃-Al composite film as cathode buffer layer. *Adv. Mater.* **24**, 2774–2779 (2012).

Acknowledgments

The authors specially thank the Analytical Engineering Group (AEG) of the Samsung Advanced Institute of Technology (SAIT).

Author contributions

S.-J.L. synthesised and analysed the materials. S.-J.L., D.-S.L., G.H.L., K.-H.L., X.B., T.Y., T.R. and M.G.H. prepared and analysed the films. D.-S.L., S.-J.L. and M.G.H. prepared, characterised, and analysed the OPDs. K.-B.P., S.-J.L., K.-S.K., C.J.H. and R.-I.S. prepared and characterised the transparent OPDs and the OPD-integrated CMOS chips. S.S., M.L. and T.-Y.L. characterised the OPD-integrated CMOS sensors. K.N., D.I. and J.J. modified and prepared the CMOS circuits. S.-J.L., D.-S.L., K.-B.P., M.G.H., Y.W.J. and S.L. organised the project and wrote the manuscript. S.L. supervised the project. All authors commented on the manuscript.

Additional information

Supplementary information accompanies this paper at <http://www.nature.com/scientificreports>

Competing financial interests: The authors declare no competing financial interests.

How to cite this article: Lim, S.-J. *et al.* Organic-on-silicon complementary metal-oxide-semiconductor colour image sensors. *Sci. Rep.* **5**, 7708; DOI:10.1038/srep07708 (2015).



This work is licensed under a Creative Commons Attribution-NonCommercial-NoDerivs 4.0 International License. The images or other third party material in this article are included in the article's Creative Commons license, unless indicated otherwise in the credit line; if the material is not included under the Creative Commons license, users will need to obtain permission from the license holder in order to reproduce the material. To view a copy of this license, visit <http://creativecommons.org/licenses/by-nc-nd/4.0/>